# Combinatorial Large-Area MoS₂/Anatase−TiO₂ Interface: A Pathway to Emergent Optical and Optoelectronic Functionalities

Tuhin Kumar Maji, Aswin J. R, Subhrajit Mukherjee, Rajath Alexander, Anirban Mondal, Sarthak Das, Rajendra Kumar Sharma, Naba Kumar Chakraborty, Kinshuk Dasgupta, Anjanashree M. R. Sharma, Ranjit Hawaldar, Manjiri Pandey, Akshay Naik, Kausik Majumdar, Samir Kumar Pal, K. V. Adarsh, Samit Kumar Ray, and Debjani Karmakar*

Read Online

ACCESS | Metrics & More | Article Recommendations | SI Supporting Information

**ABSTRACT:** The interface of transition-metal dichalcogenides (TMDCs) and high-$k$ dielectric transition-metal oxides (TMOs) had triggered umpteen discourses because of the indubitable impact of TMOs in reducing the contact resistances and restraining the Fermi-level pinning for the metal−TMDC contacts. In the present work, we focus on the unresolved tumults of large-area TMDC/TMO interfaces, grown by adopting different techniques. Here, on a pulsed laser-deposited MoS₂ thin film, a layer of TiO₂ is grown by atomic layer deposition (ALD) and pulsed laser deposition (PLD). These two different techniques emanate the layer of TiO₂ with different crystallinities, thicknesses, and interfacial morphologies, subsequently influencing the electronic and optical properties of the interfaces. Contrasting the earlier reports of n-type doping at the exfoliated MoS₂/TiO₂ interfaces, the large-area MoS₂/anatase−TiO₂ films had realized a p-type doping of the underneath MoS₂, manifesting a boost in the extent of p-type doping with increasing thickness of TiO₂, as emerged from the X-ray photoelectron spectra. Density functional analysis of the MoS₂/anatase−TiO₂ interfaces, with pristine and interfacial defect configurations, could correlate the interdependence of doping and the terminating atomic surface of TiO₂ on MoS₂. The optical properties of the interface, encompassing photoluminescence, transient absorption and $z$-scan two-photon absorption, indicate the presence of defect-induced localized midgap levels in MoS₂/TiO₂ (PLD) and a relatively defect-free interface in MoS₂/TiO₂ (ALD), corroborating nicely with the corresponding theoretical analysis. From the investigation of optical properties, we indicate that the MoS₂/TiO₂ (PLD) interface may act as a promising saturable absorber, having a significant nonlinear response for the sub-band-gap excitations. Moreover, the MoS₂/TiO₂ (PLD) interface had exemplified better phototransport properties. A potential application of MoS₂/TiO₂ (PLD) is demonstrated by the fabrication of a p-type phototransistor with the ionic-gel top gate. This endeavor to analyze and perceive the MoS₂/TiO₂ interface establishes the prospectives of large-area interfaces in the field of optics and optoelectronics.

**KEYWORDS:** *TMDC heterostructure, high-k dielectric oxide, p-type doping, electronic structure, Raman scattering, PL, nonlinear response, exciton dynamics, optoelectronics*
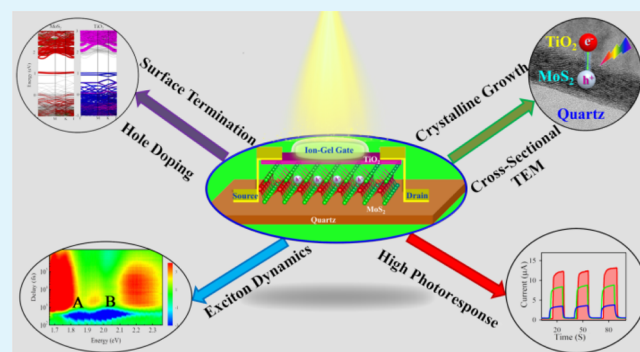
## 1. INTRODUCTION

Recent ages have discerned a surge of efforts for imprinting the superior applicability of two-dimensional (2D) materials in the field of ultrascaled logic devices over the conventional semiconductor industry materials Si or Ge. A universal set of 2D materials, embracing numerous subsets such as graphene,[1,2] silicene,[3] germanene,[4] phosphorene[5] and so forth have already manifested their better performances owing to their intrinsic physical attributes such as dangling bond-free surface containing natural passivation,[6] tunable optimal band gap,[7] advanced carrier control[8,9] and the possibility of modulating electro-optical properties by forming combinatorial van der Waals stacks.[10,11] Electronic device utilization of transition-metal dichalcogenide (TMDC) systems such as MoS₂ poses a multidisciplinary challenge to the scientific community after demanding a thorough understanding of surface and interfacial chemistry, physics of band alignment along with its
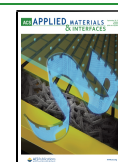
consequential impact on charge transport, and contact engineering at the metal−semiconductor interfaces.[12,13]

To attain an optimized mechanism of carrier injection and channel transport in TMDC devices, several pathways have been adopted, such as (1) tuning the contact resistances at the metal−semiconductor junction to control the metal-induced gap states (MIGSs) and Fermi-level pinning (FLP),[13−15] (2) dielectric screening of the scattering centers resulting from the interfacial carrier traps by using a high-*k* dielectric, an ionic gate, or 2D insulators[16−18] and (3) modulation of carrier density and passivation of the defect levels by substitutional doping, functionalization with chemical agents, or ionic plasma immersion.[19−22]

At metal−semiconductor junctions, the problem of high contact resistances significantly hinders their high performance, especially in the case of geometrical scaling down of device sizes. At such junctions, the Schottky barrier height (SBH = $\phi_B$) as deduced from the Schottky−Mott rule, $\phi_B = \phi_m − \chi_{sc}$, possesses a linear relationship with the metal work function $\phi_m$ and electron affinity $\chi_{sc}$ of the semiconductor.[23] In practical situations, as a result of the charge redistribution across the interface, the presence of interfacial dipoles causes a significant modification of the band bending across the interface. Thus, the modified barrier height becomes dependent on the net charge neutrality level $\phi_{CNL}$ of the semiconductor surface and the FLP factor $S$ by the relation $\phi_B = S(\phi_m − \chi_{sc}) + (1 − S)\phi_{CNL}$. This relation implies that for highly pinned systems ($S = 0$), $\phi_B$ is always fixed at $\phi_{CNL}$.[24] The FLP factor $S = \partial\phi_B/\partial\phi_m$ has an explicit relation with the interfacial density of states $D_s = (1 − S)\varepsilon_i\varepsilon_0/Sq^2\delta_i^2$, which could be modulated by the optimal thickness ($\delta_i$) of an appropriate dielectric layer with dielectric constant $\varepsilon_i$. For conventional semiconductors such as Ge[25,26] or Si,[27] the insertion of an ultrathin interlayer of high-*k* oxides between the metal and the semiconductor is considered to be the most promising expedient to assuage the FLP. This oxide layer results in a smaller SBH and lower contact resistances by dwindling both the virtual MIGS and the real interface states.[28] $TiO_2$ is well accomplished to be a suitable candidate for the interlayer, producing a significant modification of FLP for different surface geometries.[23,29]

The S-factor for $MoS_2$ is ∼0.16−0.35,[6,15,30] which is close to that for conventional semiconductors such as Ge. When used as an interfacial layer, $TiO_2$ is seen to be effective in reducing the SBH and the contact resistances at various metal−$MoS_2$ junctions.[23,31] The presence of $TiO_2$ on $MoS_2$ also has a tremendous impact on carrier mobility and scattering effects.[29] In realistic interfaces, Coulomb and point defects as well as the surface roughness act as scattering centers, which significantly influence the carrier mobility. Ideally, mobility should only be limited by phonon scattering. The presence of $TiO_2$ helps to screen the Coulomb scattering from charged impurities, reduces surface roughness, and also introduces additional remote phonon scattering.[32] All of these impacts act positively toward increasing mobility. An intermediate $TiO_2$ layer is also seen to be helpful in area-dependent carrier-transfer processes and in improving the device scalability.[33,34] Unlike the nonscalable means such as molecular and substitutional doping or passivation of defect sites, emanating nondegenerate doping[35] and a low on/off ratio, the interface engineering of $TiO_2$ has proved to be effective to obtain a significant improvement of photodetector/phototransistor performance.[36−38] In addition to $TiO_2$, various other oxides such as $MoO_3$, $WO_3$, MgO, or self-limiting surface oxides are seen to provide the surface charge-transfer doping and thus modulate the carrier density from n- to p-type in $MoS_2$,[39−41] $WSe_2$,[42] $MoTe_2$,[43] and InSe,[44,45] respectively. 2D insulators such as hexagonal boron nitride have also been utilized as an encapsulation of the TMDC layer, where it provides a tunneling barrier to modify the work function of the metals and helps to obtain low-temperature Ohmic contacts for the TMDC.[46,47] The $MOS_2/TiO_2$ interfaces are also commonly used for the betterment of photoelectrochemical and photocatalytic performances of $MoS_2$.[48,49]

Thus, the alluring interface of $MoS_2/TiO_2$ has already been thoroughly investigated from the point of view of nanoelectronic and photocatalytic device applications. However, most of the abovementioned studies are done either for micrometer-sized exfoliated flakes or for small-area chemical vapor deposition (CVD) growths of $MoS_2$, on which an amorphous ultrathin $TiO_2$ layer was deposited by atomic layer deposition (ALD). For large-area growths of both $MoS_2$ and anatase−$TiO_2$ (A−$TiO_2$), the interface is yet to be scrutinized thoroughly. Moreover, there are very few studies to analyze and compare the modulation of carrier density and the interfacial impacts of the $TiO_2$ layer with different crystallinities on the optical and optoelectronic properties of the large-area $MoS_2/A−TiO_2$ interfaces. These lacunae in the former literature provide the motivation for the current investigation.

The present work is organized as follows: First, crystalline thin films of $MoS_2$ were deposited on a quartz substrate by using pulsed laser deposition (PLD). As an overlayer, $TiO_2$ was deposited by using two different techniques, namely, PLD of A−$TiO_2$ and ALD of amorphous $TiO_2$. These two techniques lead to the formation of interfaces with different thicknesses and morphologies. Next, initial structural characterizations are done by using micro-Raman (MR) spectroscopy and cross-sectional transmission electron micrographs. The binding energy shifts of the core-level spectra of Mo 3d and S 2p for both $MoS_2/TiO_2$ (PLD) and $MoS_2/TiO_2$ (ALD) have been investigated and analyzed to obtain an indication of the type of doping of the underneath $MoS_2$. The experimental observation of doping was validated by the first-principles investigation of the $MoS_2/A−TiO_2$ interfaces, indicating that the type of doping in such kinds of TMDC/transition-metal oxide (TMO) heterostructures (HSs) has a strong dependence on the surface termination of the TMO layer. The effects of defects and acceptor levels on the properties of the HSs are also emphasized. As a next step, we have compared the optical properties of both these HSs by room-temperature and low-temperature photoluminescence (PL). The dynamical optical properties of the excited states are explored by measuring the transient absorption (TA) spectra, and the nonlinear responses are compared by *z*-scan two-photon absorption (TPA) measurements. Finally, we measured the four-probe phototransport for both these systems and then demonstrated a top-gate phototransistor from the $MoS_2/TiO_2$ (PLD) system. At the end, we summarize our results with a conclusion.

## 2. EXPERIMENTAL AND THEORETICAL DETAILS

**2.1. Experimental Details.** Commercially available $MoS_2$ (99.99% purity) and A−$TiO_2$ (99.9%) powders were finely ground, and the resulting powder was compressed to form a pellet of a diameter of 1 in. and a thickness of ∼5 mm at a pressure of 2 MPa in a uniaxial press. The pellets were then vacuum-sealed in two separate quartz cylinders at a pressure ∼$10^{−6}$ mbar. The cylinders containing $MoS_2$ and $TiO_2$ were then sintered at 800 and 1000 °C, respectively, for 5 h. After sintering, these pellets were structurally cross-checked to resemble the original phase.
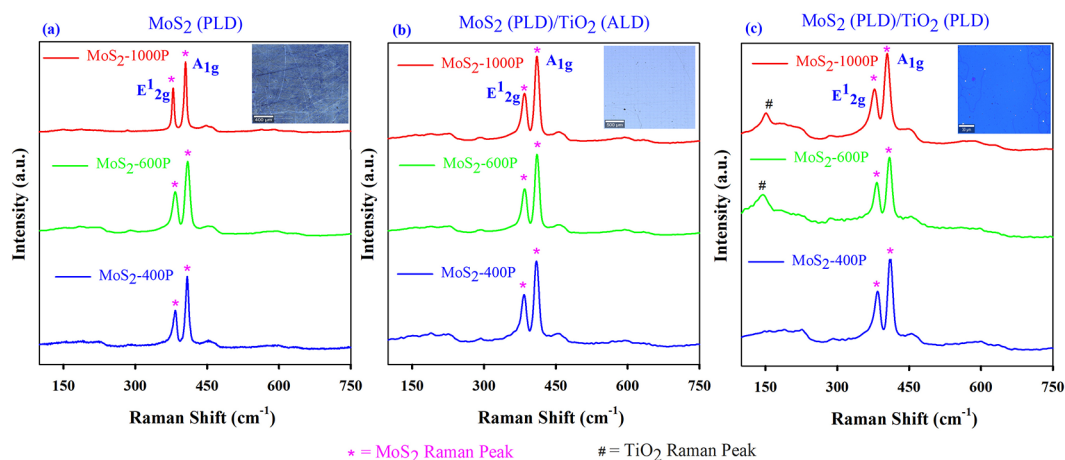
**Figure 1.** (a) MR spectra of (a) $MoS_2$ (PLD), (b) $MoS_2$ (PLD)/$TiO_2$ (ALD), and (c) $MoS_2$ (PLD)/$TiO_2$ (PLD) for different thicknesses of $MoS_2$ (400, 600, and 1000 pulses) and the same thickness of $TiO_2$ (3600 pulses) for PLD samples.

The pellets were mounted on both of the target holders of the PLD chamber. The chamber was evacuated by a combination of turbomolecular and rotary pumps to a base pressure of ~$1.33 \times 10^{-6}$ mbar. Clean quartz substrates of a size of 10 mm × 10 mm × 1 mm were mounted on the sample holder. KrF excimer laser with a wavelength of 248 nm was used for pulsed deposition. The substrate annealing temperature was kept at 650 °C. For the deposition of $MoS_2$, a repetition rate of 5 Hz and an annealing time of 5 min were used. $TiO_2$ was deposited with a repetition rate of 10 Hz with the same annealing time.

In the second set of HSs, $TiO_2$ thin films were deposited on $MoS_2$ by ALD with titanium(IV)isopropoxide (TTIP) in 25 g packages within a stainless steel cylinder. Deionized water ($H_2O$) was used as the second precursor as well. The pressure of the ALD chamber was maintained at 50 kPa, and the flow rate of the $N_2$ carrier gas was set at 20 sccm. TTIP was heated to 250 °C, and the water was kept at room temperature in order to provide sufficient vapor for the ALD process. The precursor pulse rates for TTIP and $H_2O$ were set at 0.20 and 0.15 s, respectively, with the ALD cycle sequence $H_2O$/$N_2$/TTIP/$N_2$. The deposition temperature was kept at 250 °C, and a blanket deposition of 2 nm thickness was performed with a growth per cycle of 0.04 Å/s.

High-resolution cross-sectional transmission electron micrographs were obtained with a JEOL make field emission gun transmission electron microscope (model JEM 2100F) of a magnification of 50× to 1.5M× and an accelerating potential of 200 kV. All the MR and the PL measurements are done with a 100X objective, 532 nm wavelength of laser with an appropriate exposure time.

The X-ray photoelectron spectroscopy (XPS) measurements were done at the BL-14 Beamline of RRCAT, Indore, which is used for high-resolution photoelectron spectroscopy of solids at a hard X-ray energy range (2−15 keV). In this measurement, the HSs are bombarded with high-energy X-rays and the resulting energy spectrum of emitted photoelectrons is analyzed. This spectrum is used to calculate the binding energy of the core electrons in the material, providing the elemental information and the valence configuration of the exposed surface. Although typical lab XPS provides information up to a depth of about 1 nm, high-energy XPS is capable of extracting information at larger depths as the mean free path increases with electron energy. The synchrotron source provides high-intensity X-rays over a wide range of energies, and XPS at different energies provides chemical information as a function of depth. The beamline consists of a Pt-coated toroidal mirror for focusing the X-ray beam, a double-crystal monochromator for a wide tunable X-ray energy range up to 15 keV, water-cooled X-ray slits for defining beam opening, and a high-resolution hemispherical analyzer-based experimental station for acquiring the XPS data.

In ultrafast exciton dynamics measurements, 120 fs pulses, having their center at 800 nm and with a repetition rate of 1 kHz, were divided into two beams, designated as pump and probe. The former beam is passed through an optical parametric amplifier and is considered as the

pump beam (400 nm, 120 fs pulses, and a fluence of 300 $\mu J/cm^2$). The latter beam is a white-light continuum delayed with a computer-controlled motion controller with respect to the pump. The pump and probe beams were spatially overlapped on the sample, and the change in absorbance of the probe beam $\Delta A = (\log[I_{ex}/I_0])$ was determined, where $I_0$ and $I_{ex}$ are the transmitted intensities of the sequential pump and probe pulses after a delay time $\tau$ following the excitation by the pump beam respectively.

An open-aperture $z$-scan is used to obtain a quantitative analysis of the third-order nonlinearity in terms of the analysis of the nonlinear refractive index and nonlinear absorption coefficient. In this measurement, two photodiodes are used as detectors, with one collecting the input laser energy (D1) and the other measuring the transmitted energy through the thin film (D2). By calculating the ratio of D2/D1, we have measured the normalized transmittance as a function of the sample position in a moving system with a translational stage and varying intensity profiles throughout the measurement. $z$-scan features are symmetric in nature due to the intensity profile, prepared by using a convex lens, where the maximum intensity is observed at the focal point. In the nanosecond open-aperture $z$-scan, a Nd:YAG laser of 1064 nm with a pulse width of 7 ns was used to excite the thin film under investigation. A fixed repetition rate of 10 Hz was used to avoid the damage of the thin film via the heating effect. The spot size of the beam and the Rayleigh length used in our experiment were 19 $\mu$m and 1.6 mm, respectively. The Gaussian beam was focused with the help of a 20 cm plano-convex lens of the $z$-axis of the computer-controlled translation stage.

**2.2. Computational Details.** For first-principles analysis, spin-polarized plane-wave pseudopotential calculations were performed with norm-conserving projector augmented wave pseudopotentials as implemented in the Vienna ab initio simulation package (VASP).[50] The valence levels for Mo consist of 4p, 5s, and 4d orbitals and those for S constitute 3s and 3p orbitals respectively. The exchange−correlation interactions are incorporated within the generalized gradient approximation (GGA) with Perdew−Burke−Ernzerhof (PBE) functionals after taking into account the spin−orbit coupling (SOC). Interface-induced dipolar interactions are integrated after taking care of van der Waals corrections after including a semiempirical dispersion potential to the density functional theory (DFT) energy functional following the Grimme DFT-D2 method.[51] The cutoff energy for the plane-wave expansion is set as 500 eV, and a Monkhorst−Pack grid 5 × 5 × 3 is used for Brillouin zone sampling for all calculations. The ionic positions and the lattice parameters are relaxed by using the conjugate gradient algorithm until the Hellmann−Feynman force on each ion is less than 0.01 eV.

## 3. RESULTS AND DISCUSSION

**3.1. Fabrication of the HS.** We have employed the PLD technique under ultrahigh vacuum with the vacuum-sintered target pellets of 2H-MoS$_2$ and A-TiO$_2$, respectively, for the deposition of pristine MoS$_2$ and MoS$_2$/TiO$_2$ (PLD). The thickness of the MoS$_2$ film ranges from 25 to 28 nm, which is equivalent to more than 30 layers of MoS$_2$. The number of pulses used for MoS$_2$ deposition is 400, 600, and 1000. To avoid the discrete deposition and to obtain a continuous overlayer of TiO$_2$, the number of pulses needed for the growth of TiO$_2$ is optimized to 3600, which leads to a deposition of a thickness of ~80 nm. The interface MoS$_2$/TiO$_2$ (ALD) is grown after using the cyclic gas-surface self-limiting reactions in the ALD setup for a uniform deposition of 2 nm. The details of the deposition techniques are described in the Supporting Information. In both of these cases, the surface roughness of MoS$_2$ decreases by an order of magnitude after the deposition of TiO$_2$. In the Supporting Information, the atomic force microscopy (AFM) measurement of the thickness and an estimate of the roughness for deposited thin films are described (Figure S1). Although the ALD TiO$_2$ layer is known to be amorphous,[23,38] the PLD TiO$_2$ layer is seen to be polycrystalline. The details of the thicknesses and the surface roughnesses of various systems are tabulated in Table S1.

Throughout the study, we follow the convention of designating the MoS$_2$ (PLD)/TiO$_2$ (ALD) and MoS$_2$ (PLD)/TiO$_2$ (PLD) HSs as HS1 and HS2, respectively. Moreover, HS1(1000), HS1(600), and HS1(400) imply HS1 with MoS$_2$ deposited by using 1000 pulses and so on. In a similar way, MoS$_2$(1000) indicates the MoS$_2$ PLD films deposited by using 1000 pulses.

**3.2. Structural Characterization: MR Spectroscopy and Transmission Electron Micrographs.** Figure 1a−c depicts the MR spectra of pristine MoS$_2$ (400, 600, and 1000 pulses) and the corresponding HS1 and HS2 systems upon illumination with a 532 nm green laser light. To verify the uniformity of the respective films over a large area, the spectra were produced by taking the average of several Raman mappings over a large area of 400 $\mu$m × 400 $\mu$m at various places of each film. The inset in the same figure shows the microscopic image of the corresponding thin film representing its continuous large-scale nature. Figure 1a depicts the characteristic peaks for the in-plane Mo−S vibration ($E_{2g}^1$) and the out-of-plane S vibration ($A_{1g}$) with an enhanced intensity for the latter one for pristine as well as for both of the HSs. Such an enhancement occurs because of the strong electron−phonon coupling due to resonant Raman scattering at the $K$-point, where the electrons at the $c$-axis-aligned Mo $d_{z^2}$ orbital are coupled with the phonons along the same direction because of the atomic displacements responsible for $A_{1g}$.[52] The peak positions for both of the characteristic peaks are listed in Table S2, indicating that with an increasing number of the pulses, there is an increase in the film thickness of MoS$_2$, as can be seen from the increasing difference between the $E_{2g}^1$ and $A_{1g}$ peak positions.[53] With the deposition of amorphous TiO$_2$ by ALD, the MoS$_2$ peak positions experience a blue shift, similar to the earlier study,[38] whereas with polycrystalline TiO$_2$ in PLD, there is an overall red shift, indicating the detrimental effect of the interfacial strain on both the in-plane and out-of-plane vibrations for the thicker TiO$_2$ layer. The crystalline nature of the film may have undergone a slight deterioration, as indicated by a slight increase of the full width at half-maxima after the deposition of TiO$_2$ for both HS1 and HS2. For the HS HS1, the

signature of TiO$_2$ is not visible in the MR spectra (Figure 1b), as is expected for an amorphous TiO$_2$ film.[54] On the contrary, HS1 has the signature peak of the anatase phase of TiO$_2$ at ~150 cm$^{-1}$ as a result of the better crystallinity of the TiO$_2$ layer.[54]

Figure 2 shows the cross-sectional high-resolution transmission electron microscopy (HRTEM) images for both
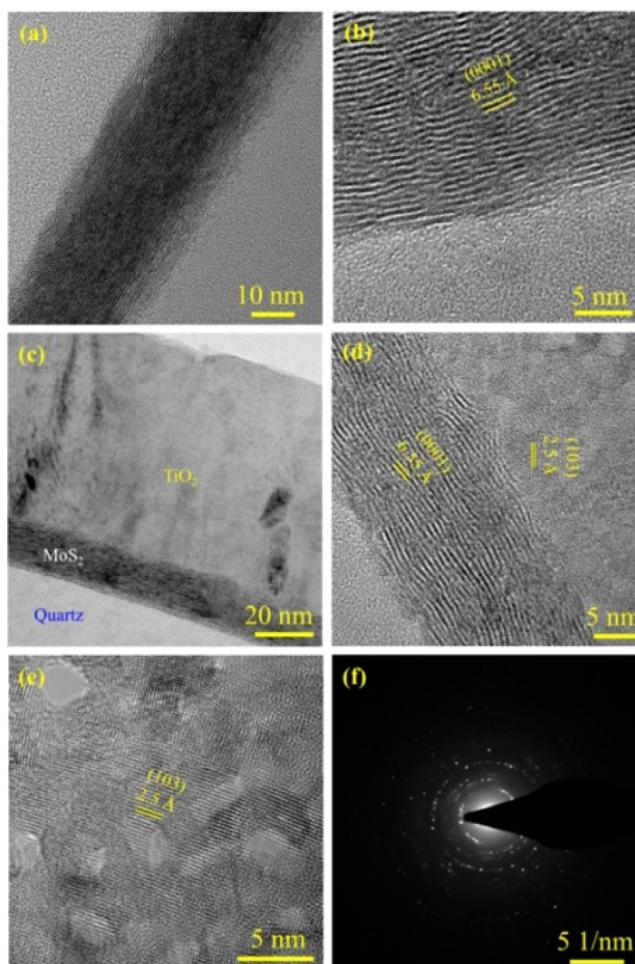


**Figure 2.** (a) Cross-sectional TEM image of PLD-grown MoS$_2$(1000), (b) HRTEM image of MoS$_2$(1000), (c) cross-sectional micrograph of HS2(1000) (see text), showing quartz, MoS$_2$, and TiO$_2$, (d) HRTEM image of HS2(1000), (e) HRTEM image of the TiO$_2$ layer of HS2(1000), and (f) SAED image of HS2(1000).

MoS$_2$(1000) and HS2(1000) films on quartz. Figure 2a clearly shows the layered nature of MoS$_2$ on quartz, where the lattice spacing, as calculated from the magnified fringe pattern of Figure 2b, is 6.55 Å, indicating a stacking along the [0001] direction.[48] Figure 2c shows the cross-sectional image of HS2 films on quartz, with different layers indicated. For the same sample, the magnified image near the MoS$_2$/TiO$_2$ interface (Figure 2d) indicates the crystalline and polycrystalline nature of the PLD-grown MoS$_2$ and A−TiO$_2$, respectively. The random orientations of the multiple grains are visible from the magnified image of the A−TiO$_2$ part of the interface in Figure 2e, where the fringe width of 2.5 Å matches with the [103] plane of A−TiO$_2$. Figure 2d also shows an uneven interface, indicating the presence of defects such as vacancies or edge boundaries. Ideally, the structure of MoS$_2$ should be devoid of any dangling bonds and carrier-trapping defect sites. However, the realistic HRTEM image of the MoS$_2$ PLD layer indicates the presence of
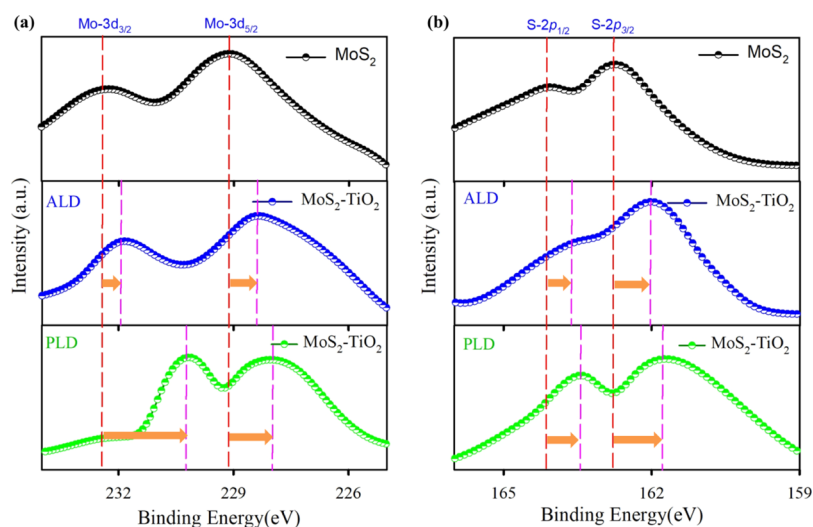
**Figure 3.** XPS spectra depicting the core-level shifts for $MoS_2$ (1000P)/$TiO_2$ systems: (a) comparison of Mo 3d levels for pristine $MoS_2$, HS1 (see text), and HS2 (see text) and (b) same comparison for S 2p levels.

discontinuous edges. These edges can be passivated by the $TiO_2$ layer, improving the overall crystallinity of the combined HS. This will also be evident from the selected area electron diffraction (SAED) images, containing both spots and the ring pattern, as seen in Figure 2f and also resembling the prior studies.[34,38]

Thus, after the fabrication of both of the proposed HSs, the structural characterizations with MR spectroscopy and transmission electron micrographs validate the synthesis of the target HSs.

**3.3. XPS: Binding Energy Shifts of Core-Level Spectra.** The standard identification technique adopted to find out the nature of doping in 2D HSs is the measurement of the binding energy (BE) shifts for the core-level electrons in the XPS spectra.[21,23,55,56] To obtain an idea of the elemental composition and the corresponding valence configuration, high-resolution photoelectron spectroscopy of the films is performed with hard X-rays in an energy range of 2−15 keV. In a similar way to the MR spectra, the resultant XPS data for each film are obtained by averaging over several scans at various places of the respective film. The details of the measurement are presented in the Supporting Information.

Figure 3 shows the comparative plots for the BE of the core levels, namely, Mo $3d_{5/2}$, Mo $3d_{3/2}$, S $2p_{3/2}$, and S $2p_{1/2}$ for the pristine $MoS_2$ and for both HS1 and HS2 with $MoS_2$ deposited with 1000 pulses. After the deposition of $TiO_2$, both the Mo 3d (Figure 3a) and S 2p (Figure 3b) doublets undergo a shift toward the lower BE for HS1 and HS2, implying a shift of the Fermi level toward the valence band and thereby indicating p-type doping. As is also evident from Figure 3, the shift of the BE and thus the extent of the p-type doping are more for HS2 (PLD-$TiO_2$) than for HS1 (ALD-$TiO_2$). The shifts of different core levels are observed to be different, which can be attributed to the nonuniformity of the $MoS_2$/$TiO_2$ interfaces, whereby the environments around the Mo and S atomic levels differ. The Supporting Information contains the comparative XPS spectra of HS1 and HS2 with the corresponding pristine system deposited with 400 and 600 pulses of $MoS_2$. For all of these HSs, the shifts of BE indicate p-type doping, which differs from the prior results in the literature for the exfoliated $MoS_2$ and ALD $TiO_2$.[23,34,38] The consolidated list of shifts in BE for different HSs is presented in Table S3.

Therefore, for both HS1 and HS2, the large-area HSs result in a p-type doping of the $MoS_2$ layer, contrary to the prior studies on exfoliated HSs. As a next step, we analyze this doping behavior with the help of first-principles calculations.

**3.4. First-Principles Study of the Interface: Correlation of Surface Termination and Doping.** To understand the doping behavior of the large-area interfaces, we have elaborately investigated the $MoS_2$/$TiO_2$ interface. There is a significant difference between the interface created from the micrometer-sized exfoliated $MoS_2$ and a fast deposition of amorphous $TiO_2$ by ALD[21,23,34,38] with the large-area epitaxial growth processes used in the present study. Since the large-area interfaces are grown with longer deposition times, there are provisions of a gradual relaxation of the interfacial strains with increasing thickness of the top layer by mutual rotation of the constituting surfaces at the interfacial region. Keeping this scenario in mind, construction of the interface is done after stacking a $(2 \times 2 \times 1)$ supercell of 2H-$MoS_2$ ($P6_3/mmc$) with a $(2 \times 2 \times 1)$ supercell of A-$TiO_2$ ($I4_1/amd$) by the coincidence site lattice method, as implemented in the Atomistic ToolKit 15.1 package.[57,58] For minimization of the mutual rotational strain of the interface, a survey was performed through the grid $mv_1 + nv_2$, with the vectors $v_1$ and $v_2$ being the basis vectors of the $MoS_2$ lattice, so that for the maximum values of the integers $m$ and $n$ (6 in the present case), the supercells of both of the lattices have the lowest mismatch. In the next step, the mutual strain is minimized by varying the relative rotational angle between the $MoS_2$ and $TiO_2$ surface cells around the stacking direction ($c$-axis for the present case) in increments of $1°$. In all of our calculations, the minimized mutual strain is ∼0.87%, while the mutual rotational angle between the two surfaces is ∼46°. The grid areas for $MoS_2$ and $TiO_2$ and their respective relative rotations are presented in Figure S4. Figure 4 shows the two possibilities of surface termination of the $TiO_2$ layer on $MoS_2$, namely, (a) O termination and (b) Ti termination.

The electronic structures of these two interfaces are investigated with the help of GGA-PBE + SOC calculations, as implemented in the VASP.[50] The details of the methodology for the formation of HSs are mentioned in the Supporting Information. We have taken care of the impact of the presence of vacancies in these two interfaces, where, for the O-terminated interface, the interfacial S (at $MoS_2$) and O (at $TiO_2$) vacancies
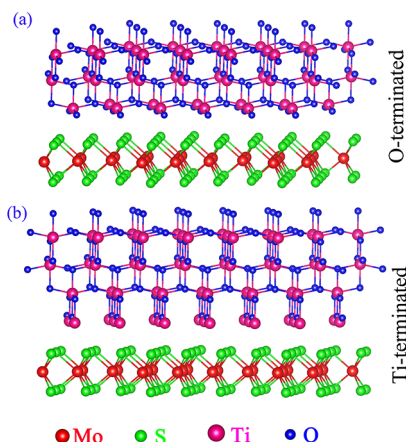
**Figure 4.** Structural image of (a) O-terminated $MoS_2$/$TiO_2$ HS and (b) Ti-terminated $MoS_2$/$TiO_2$ HS.

are designated as SV and OV, respectively. In a similar way, for the Ti-terminated one, the S (at $MoS_2$) and Ti (at $TiO_2$) vacancies are denoted as SV and TiV, respectively. The outcome of a converged calculation of the Fermi-level shifts for all these interfaces is listed in Table 1, revealing the significant impact of

**Table 1. Shift of $E_F$ vs Surface Termination for Different Systems (See Text)**

| system | shift of EF (eV) | type of doping |
|---|---|---|
| O-terminated | −0.10 | p-type |
| O-terminated + SV | −0.11 | p-type |
| O-terminated + OV | −0.12 | p-type |
| Ti-terminated | +1.53 | n-type |
| Ti-terminated + SV | +1.54 | n-type |
| Ti-terminated + TiV | +1.72 | n-type |

surface termination and the interfacial vacancies on the nature of doping. Although the Ti-terminated surfaces are heavily n-type-doped with a significant shift of $E_F$ toward the conduction band (Table 1), revealing a metallic nature, the O-terminated ones indicate p-type doping with a shift of $E_F$ toward the valence band (Table 1). Additionally, in the latter case, the system is semiconducting in one spin channel and metallic in the other one, representing a perfect half-metal. Because the experimental systems are all indicating a p-type doping, we present the results of the O-terminated interface in the main article, with the Ti-terminated details in the Supporting Information.

Figure 5 shows the layer cum orbital-projected band structure and the corresponding DOS for the pristine O-terminated interface and the same interface with SV and OV, respectively. The vertical up and down panels constitute the layer-projected $MoS_2$ and $TiO_2$ fatbands with the corresponding orbital contributions as Mo d (red), S p (green), Ti d (magenta), and O p (blue), respectively. A thorough scrutiny of the band structures indicates the following key findings:

(A) The direct-band gap resulting from the Mo d orbitals (red bands in the upper panel of Figure 5a) remains unaltered in the HS with a k-space shift of the conduction band minima (CBM) in between the $\Gamma-M$ high-symmetry directions as a result of the van der Waals interactions with the vertically stacked $TiO_2$. The overall semiconducting nature of $MoS_2$ is protected.

(B) $TiO_2$ results in the acceptor levels within ~0.5 eV of the valence band of $MoS_2$ (blue bands in the lower panel of Figure 5a) as a result of the charge transfer from the mutually rotated $MoS_2$ to $TiO_2$. It also leads to the generation of localized midgap states at ~1 eV. Interestingly, all these $TiO_2$-generated states contribute only to the upspin channel and mostly have the O p orbital character, leading to the half-metallic nature of the interface, as can also be seen from the corresponding orbital projected DOS.

(C) For $MoS_2$, there is a mixing of the Mo d and S p characters both at the valence band (VB) maxima (VBM) and at the CBM. On the other hand, for $TiO_2$, the Ti d orbital contributions are prominent at CBM with the O p orbitals contributing near VBM.

(D) In the presence of OV (Figure 5b), some additional midgap states having O p orbital characters are generated at ~1 eV only in the upspin channel, retaining the half-metallic nature. However, in the case of SV (Figure 5c), midgap levels having S p orbital characters are generated in both the spin channels.

(E) In addition to the SOC-induced splitting at the VBM, there is similar splitting of levels at the CBM too. The unequal splitting of the bands at both the band edges may lead to the occurrence of the satellite peaks adjacent to the primary excitons, as can be seen in the next section.

The corresponding Ti-terminated layer and the orbital projected band structures are presented in Figure S5. From the same figure, the heavily n-type-doped metallic nature of the interface with the near $E_F$ contribution resulting mostly from $TiO_2$ is evident. The electronic properties of prior references having exfoliated $MoS_2$ and ultrathin amorphous $TiO_2$ resemble those of this Ti-terminated structure.[23,34,38]

Figure 6a,d illustrates the converged charge and spin densities for the O-terminated interfaces, where most of the charge and spin densities are observed to be located around the $TiO_2$ layer. The $MoS_2$ layer is clearly devoid of charge, supporting the p-type nature of the interface. Remarkably, the magnetic nature of the system originates solely because of $TiO_2$. In the presence of OV (Figure 6b,e) and SV (Figure 6c,f), in spite of local reshuffling of charge and spin densities, the p-type nature of the system remains unaltered. Figure S6 shows the charge and spin densities for the Ti-terminated HS, where more overlapping charge and spin regions between the $MoS_2$ and $TiO_2$ layers upholds the n-type nature of doping obtained for the interface.

Thus, the first-principles investigations of the $MoS_2$/$TiO_2$ interface indicate the importance of surface termination and the presence of interfacial vacancies on the electronic properties of the HS.

**3.5. PL of the HSs: Impact of $TiO_2$ Deposition.** PL was measured for $MoS_2$(1000), HS1(1000), and HS2(1000) with a laser of a wavelength of 532 nm and a spot size of 20 $\mu$m diameter with the maximum power of the laser to be restricted to ~1.6 mW. In monolayer $MoS_2$, because of the SOC-induced VB splitting and the enhanced Coulomb interactions, there are multiexciton interactions surviving even at room temperature.[59,60] Even for multilayered systems, there is a symmetry-driven even and odd-layer distribution of interlayer and intralayer excitons. The intralayer excitons, having an order of magnitude higher radiative decay rate, contribute the most to the PL signal. The layer distribution of the excitons imparts their higher stability even in the bulk limit.[61] Figure 7 depicts the
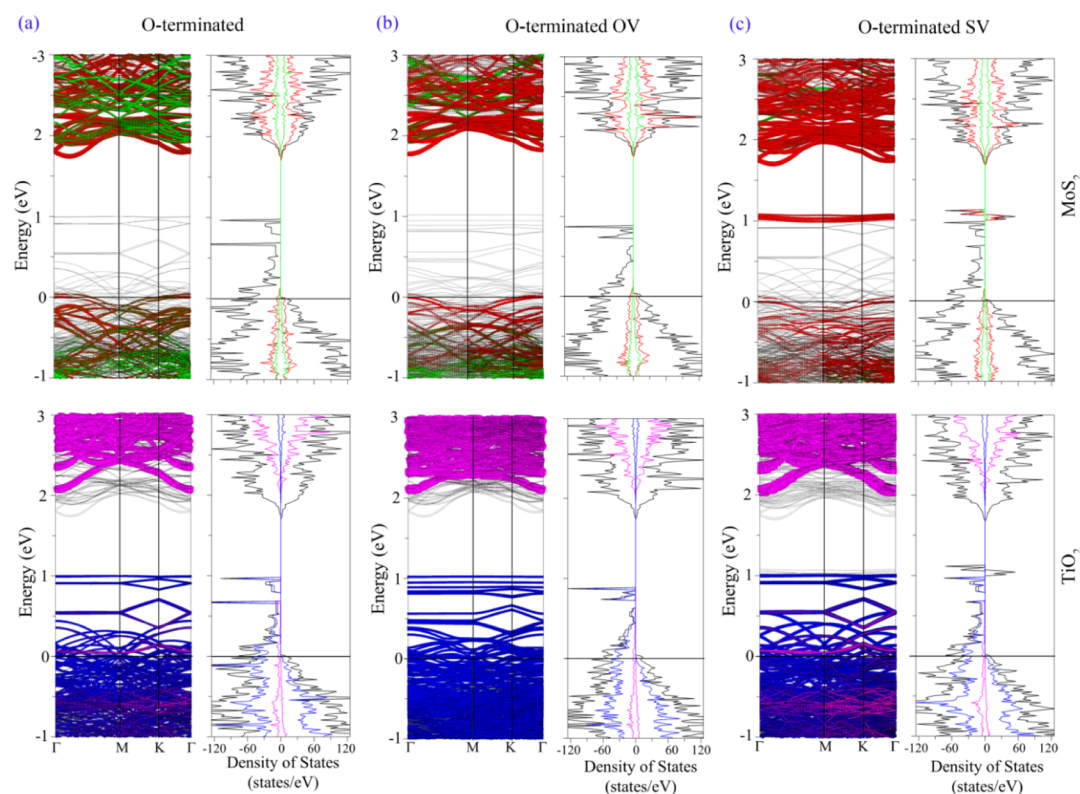
**Figure 5.** Layer-projected fatbands for $MoS_2$ (upper panel) and $TiO_2$ (lower panel) and the corresponding partial DOS for (a) O-terminated $MoS_2$–$TiO_2$ systems, (b) O-terminated $MoS_2$–$TiO_2$ systems with O vacancy (OV), and (c) O-terminated $MoS_2$–$TiO_2$ systems with S vacancy (SV). The color codes used for orbital projections are Mo d (red), S p (green), Ti d (magenta), and O-p (blue).
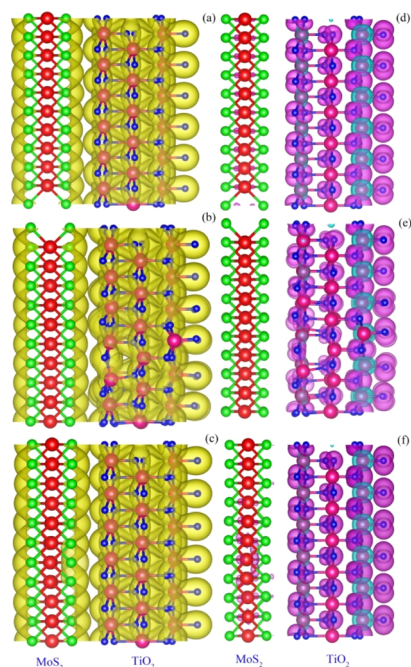


**Figure 6.** Charge densities of different systems (a) O-terminated $MoS_2/TiO_2$, (b) same with OV, and (c) same with SV and corresponding spin densities of different systems (d) O-terminated $MoS_2/TiO_2$, (e) same with OV, and (f) same with SV.

comparative PL spectra for a specific set, $MoS_2(1000)$, HS1(1000), and HS2(1000), with the general feature of an increased intensity and linewidth for the B-exciton. In prior studies on large-area $MoS_2$, there are signatures of the enhanced

intensity of the B-exciton, which are attributed to the proximity of the electron–hole pairs in the 2D systems possessing larger densities of excitons, leading to mutually driven correlated interexcitonic interactions.[62] Figure 7a shows the PL spectra of HS1(1000) (red) and pristine $MoS_2(1000)$ (green) at 300 K. Pristine $MoS_2$ reveals the A- and B-exciton peaks at ∼1.77 and ∼2.08 eV, revealing a red and blue shift in comparison to the monolayer $MoS_2$ exciton positions, respectively. These shifts can be attributed to the multilayered nature and weak van der Waals stacking due to the presence of defects and surface edges, as is also evident from the TEM images. For HS1(1000), in addition to the A- and B-excitons, there is an additional saddle-point peak ∼0.1 eV away from the B-exciton, whose presence may be ascribed to the two direct consequences of the band structure of the HS. The first is the SOC splitting at CBM and the second is the presence of $TiO_2$-generated acceptor levels, which may accommodate the deexcited electrons from CBM. Figure 7b shows a weak A-exciton peak at ∼1.79 eV and a strong B-exciton at 2.08 eV. Here, the saddle-point peak is not prominent because of the stronger B-exciton. Low-temperature (4 K) PL of both HS1 and HS2, however, reveals the prominent presence of all three peaks, namely, A-exciton (∼1.76 eV), saddle-point peak (∼1.96 eV), and B-exciton (∼2.09 eV), as is evident from the Figure 7c,d with three different laser powers. A comparison with the PL of pristine $MoS_2$ reveals an overall increase of PL intensity in the HS with HS1 (ALD) having a stronger intensity than HS2 (PLD). The Supporting Information shows a comparison of PL at 4 K with the laser focusing at different points of the HS (Figure S7).

Therefore, the room-temperature and low-temperature PL data convey the details of the origin of the excitonic interactions
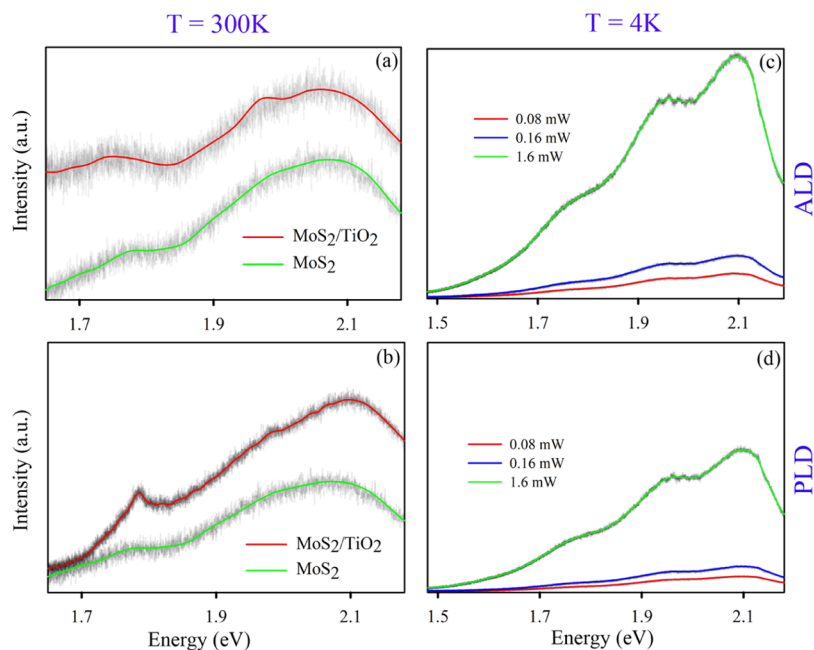
**Figure 7.** Comparative PL spectra of (a) HS1(1000) and MoS$_2$(1000) at 300 K, (b) HS2(1000) and MoS$_2$(1000) at 300 K, (c) HS1(1000) at 4 K for three different laser powers, and (d) HS2(1000) at 4 K for three different laser powers.
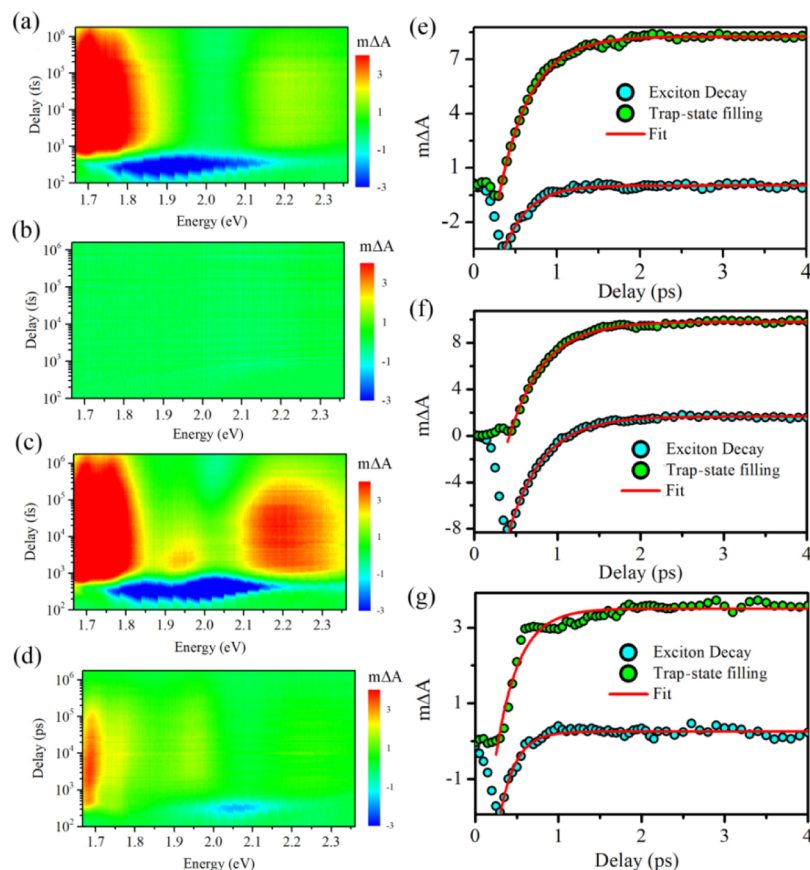


**Figure 8.** Contour plots (see text) of TA measurements for (a) MoS$_2$(1000), (b) TiO$_2$(3600), (c) HS1(1000), and (d) HS2(1000). Kinetics for A-exciton decay at 2 eV and trap-state filling at 1.73 eV for (e) MoS$_2$(1000), (f) HS1(1000), and (g) HS2(1000).

for both the HSs. In the next section, we will investigate the exciton dynamics of these HSs.

**3.6. Probing the Exciton Dynamics by TA for HSs.** The exciton dynamics of the pristine MoS$_2$ as well as the HS is probed by using ultrafast (picosecond-resolved) TA spectroscopy, in which the system is excited with a pump photon of 3.1 eV, exceeding the steady-state band gap of MoS$_2$. Next, the changes in the absorbances are measured by using a probe signal

ranging from 1.79 to 2.6 eV. Before executing the survey on the excited state, we have recorded the ground-state absorption spectrum at room temperature, as shown in Figure S8. A closer scrutiny of the overall absorbance in Figure S8 reveals the quenched nature of the A- and B-excitons in $MoS_2$ multilayered films and HS2(1000). HS1(1000) manifests more prominent A- and B-exciton features. Figure 8a−d shows the contour plot of TA for $MoS_2$(1000), $TiO_2$(3600), HS1(1000), and HS2(1000), respectively, where the pump−probe delay is plotted against the energy of the probe beam. The color codes for the contour, representing the change in the absorbance between the excited and ground states ($A_{excited} - A_{ground} = m\Delta A$, where $m = 10^{-3}$), are depicted as side bars. Figure 8e−g shows $m\Delta A$ as a function of the pump−probe delay for $MoS_2$(1000), HS1(1000), and HS2(1000), respectively. The figures show bleach at the exciton position due to the filling up of the excited state and a time delay-induced absorption below the exciton position due to the presence of the trap states. The timescales for the exciton decay and the trap-state filling are listed in Table 2. The TA contour and the kinetic plots for $MoS_2$(400) and $MoS_2$(600) and also for the corresponding HS1 and HS2 are presented in the Supporting Information.

**Table 2. Exciton Decay and Trap Buildup Times for Different Systems**

| sample | exciton decay (ps) | trap buildup (ps) |
|---|---|---|
| $MoS_2$(1000) | $0.29 \pm 0.01$ | $0.33 \pm 0.01$ |
| HS1(1000) | $0.41 \pm 0.01$ | $0.42 \pm 0.01$ |
| HS2(1000) | $0.19 \pm 0.01$ | $0.22 \pm 0.02$ |

$MoS_2$(1000), being an indirect band-gap system, shows a broad exciton band, where the A- and B-excitons merge ranging from 1.75 to 2.21 eV (Figure 8a). The exciton decay is followed by the trap-state absorption at ∼1.69 eV. The exciton decay time ($0.29 \pm 0.01$ fs) is smaller than the trap-state buildup time ($0.33 \pm 0.01$ fs). In $MoS_2$, the presence of SV-induced midgap trap states is well known.[20,63] Although $TiO_2$ is devoid of any exciton band (Figure 8b), for HS1(1000) (Figure 8c), well-resolved A- and B-excitons are observed with larger intensity for B-excitons, resembling well with the PL behavior. Additionally, there is an escalation of the sub-band-gap as well as higher-energy delocalized trap states after the decay of excitons, which implies that after the dissociation of excitons, the carriers may be transported from $MoS_2$ to the delocalized acceptor levels of $TiO_2$ near the VB. On the other hand, for HS2(1000) (Figure 8d), exciton signals are highly quenched, implying the depletion of carriers from $MoS_2$ to $TiO_2$, supporting a stronger p-type doping behavior. The localized mid-gap traps are also observed in HS2(1000), resembling the band structure of both pristine HS as well as in the presence of OV and SV (Figure 5). Therefore, HS1 manifests a longer lifetime of excitons than HS2, as also seen in Table 2, which can be imputed to the presence of the larger interlayer charge transfer and greater density of midgap traps. Figures S9 and S10 show a similar behavior for other HSs too. The comparative TA spectra recorded with a delay of 2 ps also show a similar behavior, as shown in Figure S8c. In the next section, we examined the presence of the midgap traps, which is responsible for the quenching of excitons, in different HSs after comparison with the pristine system with the help of z-scan TPA measurements.

Thus, the interdependence of midgap trap states and the manifestation of exciton signals for these two types of HSs

provide an idea about the presence of vacancies and their respective densities at the interfacial region.

**3.7. Nonlinear Response in the HS: Effective TPA Measurements.** Nanosecond-resolved open-aperture z-scan measurements are performed on the same systems as in the previous section, namely, $MoS_2$(1000), HS1(1000), and HS2(1000), to study the quantitative analysis of the third-order nonlinearity and to analyze the possibility of midgap states. In this measurement, the normalized transmittance was recorded as a function of the sample positions.

In this measurement, we purposely concentrate on exciting the system with sub-band-gap 1064 nm near-infrared excitation and thereby compare the possibilities of TPA for different HSs. Higher intensities of below band-gap excitations indicate higher densities of the midgap levels, which can be attributed to the presence of vacancies in the respective HS. Figure 9a shows the
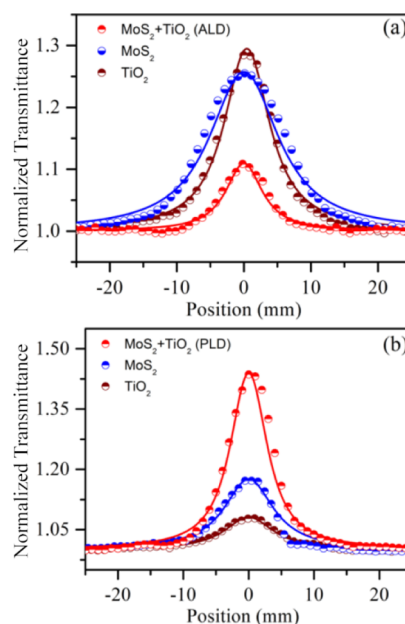


**Figure 9.** Comparative normalized transmittance as a function of position in the open-aperture z-scan at a peak intensity of 15 MW/cm² at 7 ns and 1064 nm pulse excitation for (a) HS1(1000), $MoS_2$(1000), and $TiO_2$(3600) and (b) HS2(1000), $MoS_2$(1000), and $TiO_2$(3600). The solid lines represent theoretical fitting.

normalized transmittance as a function of z-scan positions for $MoS_2$(1000), $TiO_2$(3600), and HS1(1000), with a peak intensity of 15 MW/cm². For both $MoS_2$ and $TiO_2$, 1064 nm corresponds to a sub-band-gap excitation and Figure 9a displays a monotonous increase of the normalized transmittance till the focal point ($z = 0$), representing a typical feature of the saturable absorption (SA) for both systems.[63,64] However, HS1(1000) indicates highly reduced SA, as compared to both $TiO_2$ and $MoS_2$, as shown in Figure 9a. Such behavior corroborates nicely with the unquenched exciton signals for HS1(1000), indicating a lower density of midgap traps. On the other hand, Figure 9b, showing a similar comparison for HS2(1000), manifests a significant enhancement of SA and thereby indicates the presence of effective TPA in this system. This enhancement of SA due to the presence of effective TPA indicates the presence of midgap states within HS2(1000), providing intermediate levels for TPA. This behavior goes hand in hand with the TA exciton dynamics, where the exciton signals were highly quenched for
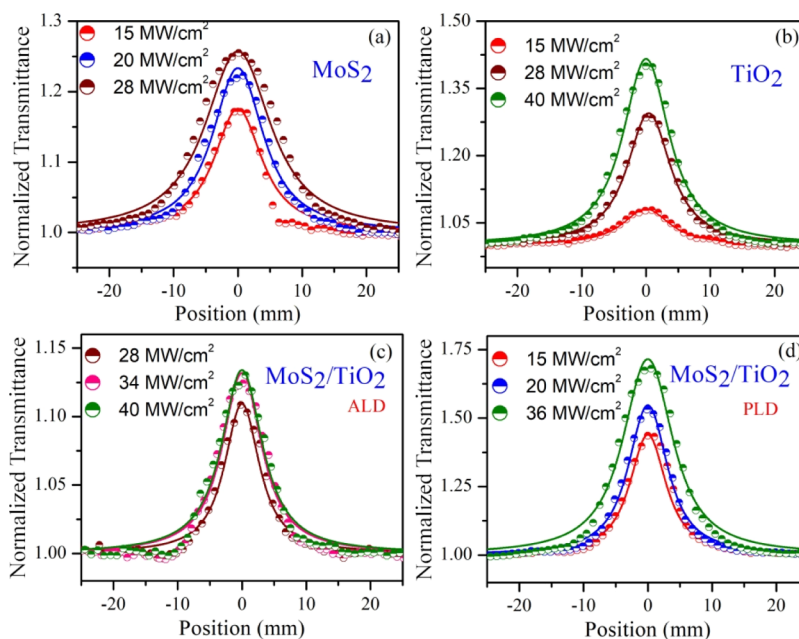
**Figure 10.** Normalized transmittance as a function of position in the open-aperture z-scan at 7 ns and 1064 nm pulse excitation with different peak intensities for (a) MoS$_2$, (b) TiO$_2$, (c) MoS$_2$/TiO$_2$ (ALD) (HS1), and (d) MoS$_2$/TiO$_2$ (PLD) (HS2), respectively.
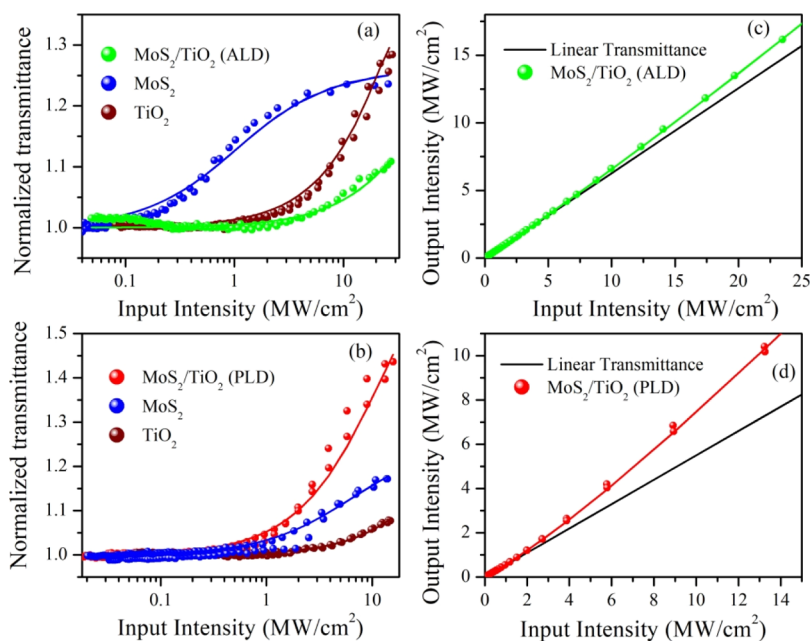


**Figure 11.** Comparison of normalized transmittances as a function of input intensity for (a) HS1(1000) and (b) HS2(1000) at 1064 nm excitation. Here, the symbols and solid curves represent the experimental data and theoretical fits, respectively. Optical limiting curve represented by the variation of output intensity as a function of input intensity for (c) HS1(1000) and (d) HS2(1000). The black line shows the linear transmittance and the curved lines represent the theoretical fits.

HS2(1000) because of the depletion of carriers from MoS$_2$ and their subsequent transfer to TiO$_2$. Thus, the presence of midgap states, as indicated by the quenching of excitons, is also verified by the z-scan measurements.

The normalized transmittances for different peak intensities are plotted in Figure 10 for (a) MoS$_2$(1000), (b) TiO$_2$(3600), (c) HS1(1000), and (d) HS2(1000). For MoS$_2$, TiO$_2$, and HS2, the monotonic power dependence is very obvious. However, for HS1(1000), the plotted transmittances have little dependence on different powers because of the reduced extent of TPA. A comparison of the normalized transmittances as a function of the

input intensity is plotted in Figure 11 for (a) HS1(1000) and (b) HS2(1000) at 1064 nm excitation. The optical limiting curve, represented by the variation of the output intensity as a function of input intensity, is plotted in Figure 11 for HS1(1000) (Figure 11a,b) and for HS2(1000) (Figure 11c,d). The black line shows the linear transmittance and the curved lines represent the theoretically fitted curve. It is evident from the figure that HS2 has a more prominent nonlinearity than HS1. A high thickness of the TiO$_2$ layer in HS2 may be a reason for this increased nonlinearity.

Thus, among both the HSs, PLD-grown HS2(1000) acts as a better potential saturable absorber material having a prominent nonlinear response for the sub-band-gap (1064 nm) excitation.

**3.8. Application in Four-Probe Phototransport and Large-Area Optoelectronics.** The resultant outcome of the previous sections implies p-type doping for both HS1 and HS2 with the extent of doping being more for HS2. To analyze the applicability of such a large-area HS for optoelectronic applications, we have measured the four-probe phototransport and later have analyzed its potential for the phototransistor applications.

On $MoS_2(1000)$, HS1(1000), and HS2(1000) films, Ni contacts of a diameter 500 $\mu$m are deposited by thermal evaporation after using a shadow mask array. Earlier reports[65] indicated a betterment of SBHs by using Ni contacts. Figure 12
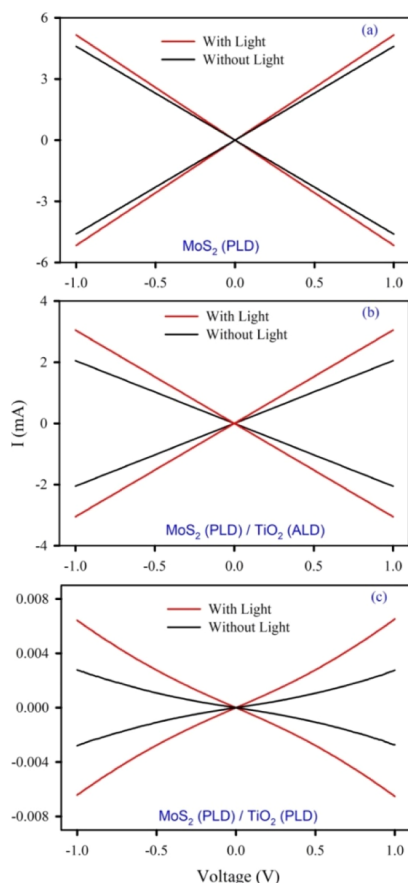


**Figure 12.** Four-probe $I$-vs-$V$ characteristics of different systems: (a) $MoS_2(1000)$, (b) HS1(1000), and (c) HS2(1000).

depicts the results of four-probe phototransport measurements for these three systems, where channel-width normalized currents (in mA) are plotted as a function of voltages (in volts). The linear current-versus-voltage behavior confirms the Ohmic nature of the Ni contact for the first two cases. However, for HS2(1000), with increasing voltage, the characteristics become nonlinear. A closer comparison shows that the reduction of current in HS1(1000) is not much significant in comparison to that in $MoS_2(1000)$, whereas there is 3 orders of magnitude reduction in the case of HS2(1000). Under illumination, $MoS_2(1000)$ does not demonstrate much improvement of photogenerated carriers, as is expected for multilayered systems. However, for both HS1 and HS2, there is

a significant improvement of the photogenerated carriers, with the latter having a better photoresponse. Theoretically, we have established the presence of acceptor level-induced p-type doping and a direct band-gap nature for such an HS. The present result of an improved photoresponse tallies well with the theoretical prediction. As a next step, we have analyzed the potential of the $MoS_2/TiO_2$ large-area HS in producing a large-area photo-transistor by fabricating a top-gated device by using the ionic gel as a gate. Because the PLD HS has shown the maximal photoresponse, the device applicability is tested for HS2.

Room-temperature ionic liquids are well known[66−68] for their potential applications as a dielectric gate for controlling the electronic properties of semiconductors. Usually, field-effect transistors (FETs) are designed after using oxide gate dielectrics, offering high operating voltage windows and higher power consumption, rendering them inappropriate for modern-age low-power integrated electronics. The ion-gel dielectric-gated FET can overcome these limitations by forming electric double-layer (EDL) capacitors under an external electric field because of its large specific capacitance ($>1$ $\mu$F·cm$^{-2}$).[67]

We demonstrate a low-operating-voltage EDL FET based on HS2(1000) after using ion-gel gate dielectrics and analyze their photoresponse characteristics by simultaneous illumination and gate bias. The device fabrication and the measurement details are presented in the Supporting Information. Polyethylene oxide and lithium perchlorate ($LiClO_4$) precursors are used to prepare the gate dielectrics.

Figure 13a shows the transfer characteristics ($I_d−V_g$ curves) of the fabricated transistor, measured at a fixed drain−source bias ($V_d$) of 1 V, exhibiting a typical FET behavior. Interestingly, the resulting device exhibits a signature of the p-type channel characteristics, predominantly indicating a hole transport through the HS2(1000) channel, which is different from the 2D-$MoS_2$-based n-type FET channel behavior. The off-state current ($I_{off}$) of the FET is ~0.53 $\mu$A, and the channel current increases sharply, leading to an ON condition, as $V_g$ decreases below a threshold voltage ($V_{th}$) of −3.5 V and then saturates at ~37 $\mu$A ($I_{on}$) after a gate bias of ~−18 V. The low turn-on voltage (−3.5 V) of the fabricated FET, which can be ascribed to the high specific capacitance of the dielectric ion gel, allows the work function of the channel to be readily modulated at low operating voltages. The resulting on/off ratio ($I_{on}/I_{off}$) is found to be ~75 in operating voltages between −20 and 5 V.

Under the application of a negative gate bias ($V_g$) to the channel material ($MoS_2/TiO_2$), the resultant electric field drives the $Li^+$ ions toward the gate electrode and the $ClO_4^-$ ions near the channel surface, forming a nanoscale thickness gate capacitor, known as an EDL. The large capacitance of the EDL, leading to a large surface carrier density and induced holes in the p-type channel, effectively enhances the electric current through the channel between source and drain electrodes. The field-effect mobility has been determined by using the expression, $\mu = \Delta I_d/\Delta V_g \times L/WC_{sp}V_d$, where $L$ is the channel length (1 mm), $W$ is the channel width (2 mm), and $C_{sp}$ is the specific capacitance of the dielectric gel, which is about ~3 $\mu$F/cm$^2$.[68] From the data shown in Figure 1a, the field-effect mobility was estimated as ~3.66 cm$^2$ V$^{-1}$ s$^{-1}$. The output characteristics ($I_d$ vs $V_d$) of the ion-gel-gated $TiO_2−MoS_2$ HS FET are measured for different fixed gate voltages ($V_g$) and shown in Figure 13b. The large degree of current modulation in the device, obtained after changing the $V_g$ values, indicates that the field-effect behavior of the fabricated transistor is dominated by the HS2(1000) channel and not by the contacts.
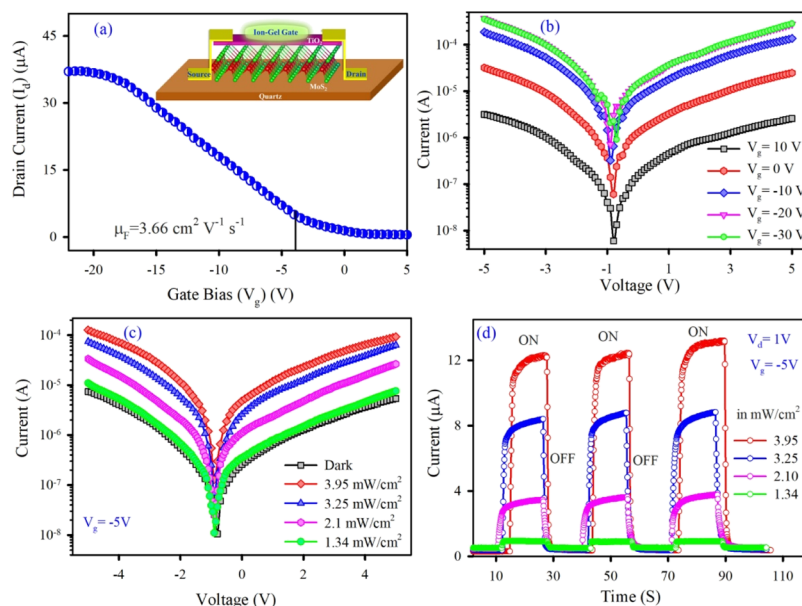
**Figure 13.** Phototransistor characteristics of large-area devices from the HS. (a) Drain current vs gate voltage characteristics implicating a p-type nature, (b) drain current vs channel voltage plot for different gate biases, (c) current vs voltage photoresponse under the dark and different illuminating conditions, and (d) phototransistor on−off behavior with different illuminating powers.

The current−voltage ($I_d$−$V_d$) characteristics of the fabricated device for a fixed gate bias ($-V_g > V_{th}$) are shown in Figure 13c under the dark and various illuminating powers. The symmetric $I$−$V$ nature indicates the formation of a similar junction between Au and the HS2(1000) hybrid at both the source and drain end. A significant increase of the current level, upon 325 nm monochromatic UV illumination, is due to the photogenerated carriers, leading to the enhancement of the field-effect mobility in the channel. The synergic effect of the dielectric gate and UV illumination results in a substantial enhancement (∼10 times) of the dark current for $V_d > \pm2$ V. The photoswitching characteristics of the fabricated EDL FET photodetector, upon pulsed illumination (with a 325 nm laser) with various power densities, have been recorded at $V_d = 1$ V and $V_g = -5$ V ($>V_{th}$), and the results are shown in Figure 13d. The rapid and periodic changes in the current level for dark and illuminated conditions represent excellent reproducibility and stability of the photodetectors. The results also demonstrate the absence of a persistent photocurrent and nonfluctuating current level with time. Moreover, the photocurrent response has been increased with increasing illumination intensity. The variation of photocurrent with incident optical intensity has been estimated and observed to display a monotonic increase with incident power, as shown in Figure S11, suggesting that the rate of photocarrier generation is proportional to the absorbed photon flux. The responsivity, a key feature of a photodetector, was calculated for a 3.95 mW/cm$^2$ (at a 325 nm laser wavelength) illumination intensity and is found to be ∼3025 A/W, indicating its superiority for millimeter-scale devices.

Thus, in the EDL FET device, electron−hole pairs are generated in the HS2(1000) channel under illumination and EDL-induced positive charges in the channel, which, through the capacitive coupling of the applied negative gate bias, effectively increases the carrier concentration, leading to an enhanced photocurrent. The gate bias is also advantageous to the neutralization of the charged vacancies, which in turn reduces the potential scattering, leading to the enhanced field-

effect mobility, resulting in an efficient collection of photocarriers.

Therefore, our results provide an important step toward the realization of the solution-processed, room-temperature deposition of high-capacitance ion-gel dielectrics integrated with 2D-HS-based millimeter-scale FETs for low-power optoelectronic applications.

## 4. CONCLUSIONS

This consolidated study demonstrates the electronic and optical impacts of different growth techniques on large-area interfaces of $MoS_2$/A-$TiO_2$ HSs. Although PLD produces a polycrystalline $TiO_2$ layer with an enhanced thickness, ALD results in an amorphous and thinner $TiO_2$ layer. Remarkably, both these interfaces emanate p-type doping of the $MoS_2$ underlayer with the increasing trend of the extent of doping with the thickness of the $TiO_2$ layer. The resulting p-type doping is validated by the first-principles investigation by demonstrating the impact of the terminating atomic layer of $TiO_2$ on $MoS_2$ and the interfacial vacancies. Substantiating the theoretical results, the steady-state and ultrafast optical responses demonstrate that the $MoS_2$/$TiO_2$ (ALD) interface is relatively free of midgap localized trap states, having clear signatures of both A- and B-excitons of $MoS_2$. The $MoS_2$/$TiO_2$ (PLD) interface, on the other hand, has significantly quenched excitons because of a higher density of localized traps. The z-scan TPA of these two interfaces indicates the application of the $MoS_2$ (PLD)/$TiO_2$ (PLD) interface as a potential saturable absorber having a significant nonlinear response. The same interface also exhibits a better photoresponse, and as an application, we have demonstrated the utilization of this interface in large-area phototransistors having significant hole mobility and photoresponse. In conclusion, with the help of both theoretical and experimental investigations, we have thoroughly scrutinized the different types of large-area interfaces of $MoS_2$/$TiO_2$ by means of different optical and transport studies and at the end demonstrated their applications as a potential phototransistor material.

## ASSOCIATED CONTENT

### ⓈⒾ Supporting Information

The Supporting Information is available free of charge at https://pubs.acs.org/doi/10.1021/acsami.0c13342.

Details of the formation of HS stacks, DFT results of the Ti-terminated interface, details of thickness and roughness measurements by AFM, additional data for different HSs including XPS, PL, TA, and TPA measurements, details of the phototransistor device-fabrication process and thickness and roughness measurements, Raman peak positions, peak shifts of XPS data, and timescales for TA (PDF)

## AUTHOR INFORMATION

### Corresponding Author

**Debjani Karmakar** — *Technical Physics Division, Bhabha Atomic Research Centre, Mumbai 400085, India;* Ⓞ orcid.org/0000-0002-9619-9493; Email: debjan@barc.gov.in

### Authors

**Tuhin Kumar Maji** — *Department of Chemical Biological and Macromolecular Sciences, S. N. Bose National Centre for Basic Sciences, Kolkata 700106, India*

**Aswin J. R** — *Department of Physics, Indian Institute of Science Education and Research, Bhopal 462066, India*

**Subhrajit Mukherjee** — *Department of Physics, IIT Kharagpur, Kharagpur, West Bengal 721302, India*

**Rajath Alexander** — *Advanced Carbon Materials Section, Bhabha Atomic Research Centre, Mumbai 400085, India*

**Anirban Mondal** — *Department of Physics, Indian Institute of Science Education and Research, Bhopal 462066, India*

**Sarthak Das** — *Department of Electrical Communication Engineering, Indian Institute of Science, Bangalore 560012, India;* Ⓞ orcid.org/0000-0001-9526-9819

**Rajendra Kumar Sharma** — *Raja Rammana Centre for Advance Technology, Indore, Madhya Pradesh 45201, India*

**Naba Kumar Chakraborty** — *Material Science Division, Bhabha Atomic Research Centre, Mumbai 400085, India*

**Kinshuk Dasgupta** — *Advanced Carbon Materials Section, Bhabha Atomic Research Centre, Mumbai 400085, India*

**Anjanashree M. R. Sharma** — *Centre for Nano Science and Engineering, Indian Institute of Science, Bangalore, Karnataka 560012, India*

**Ranjit Hawaldar** — *Centre for Materials for Electronics Technology, Pune 411008, India*

**Manjiri Pandey** — *Accelerator Control Division, Bhabha Atomic Research Centre, Mumbai 400085, India*

**Akshay Naik** — *Centre for Nano Science and Engineering, Indian Institute of Science, Bangalore, Karnataka 560012, India;* Ⓞ orcid.org/0000-0001-6325-7231

**Kausik Majumdar** — *Department of Electrical Communication Engineering, Indian Institute of Science, Bangalore 560012, India;* Ⓞ orcid.org/0000-0002-6544-7829

**Samir Kumar Pal** — *Department of Chemical Biological and Macromolecular Sciences, S. N. Bose National Centre for Basic Sciences, Kolkata 700106, India*

**K. V. Adarsh** — *Department of Physics, Indian Institute of Science Education and Research, Bhopal 462066, India*

**Samit Kumar Ray** — *Department of Chemical Biological and Macromolecular Sciences, S. N. Bose National Centre for Basic Sciences, Kolkata 700106, India; Department of Physics, IIT Kharagpur, Kharagpur, West Bengal 721302, India*

Complete contact information is available at:
https://pubs.acs.org/10.1021/acsami.0c13342

### Notes

The authors declare no competing financial interest.

## REFERENCES

(1) Novoselov, K. S.; Geim, A. K.; Morozov, S. V.; Jiang, D.; Zhang, Y.; Dubonos, S. V.; Grigorieva, I. V.; Firsov, A. A. Electric Field Effect in Atomically Thin Carbon Films. *Science* **2004**, *306*, 666−669.

(2) Andleeb, S.; Eom, J.; Rauf Naz, N.; Singh, A. K. MoS2 Field-Effect Transistor with Graphene Contacts. *J. Mater. Chem. C* **2017**, *5*, 8308−8314.

(3) Kharadi, M. A.; Malik, G. F. A.; Shah, K. A.; Khanday, F. A. Sub-10-nm Silicene Nanoribbon Field Effect Transistor. *IEEE Trans. Electron Devices* **2019**, *66*, 4976−4981.

(4) Bayani, A. H.; Dideban, D.; Vali, M.; Moezi, N. Germanene Nanoribbon Tunneling Field Effect Transistor (GeNR-TFET) with a 10 nm Channel Length: Analog Performance, Doping and Temperature Effects. *Semicond. Sci. Technol.* **2016**, *31*, 045009.

(5) Li, L.; Yu, Y.; Ye, G. J.; Ge, Q.; Ou, X.; Wu, H.; Feng, D.; Chen, X. H.; Zhang, Y. Black Phosphorus Field-Effect Transistors. *Nat. Nanotechnol.* **2014**, *9*, 372−377.

(6) Kang, J.; Liu, W.; Sarkar, D.; Jena, D.; Banerjee, K. Computational Study of Metal Contacts to Monolayer Transition-Metal Dichalcogenide Semiconductors. *Phys. Rev. X* **2014**, *4*, 031005.

(7) Chhowalla, M.; Shin, H. S.; Eda, G.; Li, L.-J.; Loh, K. P.; Zhang, H. The Chemistry of Two-Dimensional Layered Transition Metal Dichalcogenide Nanosheets. *Nat. Chem.* **2013**, *5*, 263.

(8) Fiori, G.; Bonaccorso, F.; Iannaccone, G.; Palacios, T.; Neumaier, D.; Seabaugh, A.; Banerjee, S. K.; Colombo, L. Electronics Based on Two-Dimensional Materials. *Nat. Nanotechnol.* **2014**, *9*, 768−779.

(9) Baugher, B. W. H.; Churchill, H. O. H.; Yang, Y.; Jarillo-Herrero, P. Intrinsic Electronic Transport Properties of High-Quality Monolayer and Bilayer MoS2. *Nano Lett.* **2013**, *13*, 4212−4216.

(10) Maji, T. K.; Vaibhav, K.; Pal, S. K.; Majumdar, K.; Adarsh, K. V.; Karmakar, D. Intricate Modulation of Interlayer Coupling at The Graphene Oxide/MoSe2 Interface: Application in Time-Dependent Optics and Device Transport. *Phys. Rev. B* **2019**, *99*, 115309.

(11) Geim, A. K.; Grigorieva, I. V. Van der Waals heterostructures. *Nature* **2013**, *499*, 419−425.

(12) Wang, Y.; Kim, J. C.; Wu, R. J.; Martinez, J.; Song, X.; Yang, J.; Zhao, F.; Mkhoyan, A.; Jeong, H. Y.; Chhowalla, M. Van der Waals Contacts between Three-Dimensional Metals and Two-Dimensional Semiconductors. *Nature* **2019**, *568*, 70−74.

(13) Kim, C.; Moon, I.; Lee, D.; Choi, M. S.; Ahmed, F.; Nam, S.; Cho, Y.; Shin, H.-J.; Park, S.; Yoo, W. J. Fermi Level Pinning at Electrical Metal Contacts of Monolayer Molybdenum Dichalcogenides. *ACS Nano* **2017**, *11*, 1588−1596.

(14) Li, S.-L.; Tsukagoshi, K.; Orgiu, E.; Samorì, P. Charge Transport and Mobility Engineering in Two-Dimensional Transition Metal Chalcogenide Semiconductors. *Chem. Soc. Rev.* **2016**, *45*, 118−151.

(15) Das, S.; Chen, H.-Y.; Penumatcha, A. V.; Appenzeller, J. High Performance Multilayer MoS2 Transistors with Scandium Contacts. *Nano Lett.* **2013**, *13*, 100−105.

(16) Illarionov, Y. Y.; Rzepa, G.; Waltl, M.; Knobloch, T.; Grill, A.; Furchi, M. M.; Mueller, T.; Grasser, T. The Role of Charge Trapping in MoS2/SiO2 and MoS2/hBN Field-Effect Transistors. *2D Mater.* **2016**, *3*, 035004.

(17) Dolui, K.; Rungger, I.; Sanvito, S. Origin of the n-type and p-type Conductivity of MoS2 Monolayers on a SiO2 Substrate. *Phys. Rev. B: Condens. Matter Mater. Phys.* **2013**, *87*, 165402.

(18) Bao, W.; Cai, X.; Kim, D.; Sridhara, K.; Fuhrer, M. S. High Mobility Ambipolar MoS2 Field-Effect Transistors: Substrate and Dielectric Effects. *Appl. Phys. Lett.* **2013**, *102*, 042104.

(19) Maji, T. K.; Bagchi, D.; Kar, P.; Karmakar, D.; Pal, S. K. Enhanced Charge Separation through Modulation of Defect-State in Wide Band-gap Semiconductor for Potential Photocatalysis Application: Ultrafast Spectroscopy and Computational Studies. *J. Photochem. Photobiol., A* **2017**, *332*, 391−398.

(20) Karmakar, D.; Halder, R.; Padma, N.; Abraham, G.; Vaibhav, K.; Ghosh, M.; Kaur, M.; Bhattacharya, D.; Chandrasekhar Rao, T. V. Optimal Electron Irradiation as a Tool for Functionalization of MoS2: Theoretical and Experimental Investigation. *J. Appl. Phys.* **2015**, *117*, 135701.

(21) Nipane, A.; Karmakar, D.; Kaushik, N.; Karande, S.; Lodha, S. Few-Layer MoS2 p-type Devices Enabled by Selective Doping using Low Energy Phosphorus Implantation. *ACS Nano* **2016**, *10*, 2128−2137.

(22) Srinivas, V.; Barik, S. K.; Bodo, B.; Karmakar, D.; Chandrasekhar Rao, T. V. Magnetic and Electrical Properties of Oxygen Stabilized Nickel Nanofibers Prepared by the Borohydride Reduction Method. *J. Magn. Magn. Mater.* **2008**, *320*, 788−795.

(23) Kaushik, N.; Karmakar, D.; Nipane, A.; Karande, S.; Lodha, S. Interfacial n-Doping Using an Ultrathin TiO2 Layer for Contact Resistance Reduction in MoS2. *ACS Appl. Mater. Interfaces* **2016**, *8*, 256−263.

(24) Cowley, A. M.; Sze, S. M. Surface States and Barrier Height of Metal-Semiconductor Systems. *J. Appl. Phys.* **1965**, *36*, 3212−3220.

(25) Kim, G.-S.; Kim, S.-H.; Lee, T. I.; Cho, B. J.; Choi, C.; Shin, C.; Shim, J. H.; Kim, J.; Yu, H.-Y. Fermi-Level Unpinning Technique with Excellent Thermal Stability for n-Type Germanium. *ACS Appl. Mater. Interfaces* **2017**, *9*, 35988−35997.

(26) Kim, G.-S.; Lee, T. I.; Cho, B. J.; Yu, H.-Y. Schottky Barrier Height Modulation of Metal−Interlayer−Semiconductor Structure Depending on Contact Surface Orientation for Multi-Gate Transistors. *Appl. Phys. Lett.* **2019**, *114*, 012102.

(27) Agrawal, A.; Lin, J.; Barth, M.; White, R.; Zheng, B.; Chopra, S.; Gupta, S.; Wang, K.; Gelatos, J.; Mohney, S. E.; Datta, S. Fermi Level Depinning and Contact Resistivity Reduction using a Reduced Titania Interlayer in n-Silicon Metal-Insulator-Semiconductor Ohmic Contacts. *Appl. Phys. Lett.* **2014**, *104*, 112101.

(28) Kim, G.-S.; Kim, S.-W.; Kim, S.-H.; Park, J.; Seo, Y.; Cho, B. J.; Shin, C.; Shim, J. H.; Yu, H.-Y. Effective Schottky Barrier Height Lowering of Metal/n-Ge with a TiO2/GeO2 Interlayer Stack. *ACS Appl. Mater. Interfaces* **2016**, *8*, 35419−35425.

(29) Zhao, Y.; Xu, K.; Pan, F.; Zhou, C.; Zhou, F.; Chai, Y. Doping, Contact and Interface Engineering of Two-Dimensional Layered Transition Metal Dichalcogenides Transistors. *Adv. Funct. Mater.* **2017**, *27*, 1603484.

(30) Kang, J.; Liu, W.; Banerjee, K. High-Performance MoS2 Transistors with Low-Resistance Molybdenum Contacts. *Appl. Phys. Lett.* **2014**, *104*, 093106.

(31) Freedy, K. M.; Olson, D. H.; Hopkins, P. E.; McDonnell, S. J. Titanium Contacts to MoS2 with Interfacial Oxide: Interface Chemistry and Thermal Transport. *Phys. Rev. Mater.* **2019**, *3*, 104001.

(32) Yu, Z.; Pan, Y.; Shen, Y.; Wang, Z.; Ong, Z.-Y.; Xu, T.; Xin, R.; Pan, L.; Wang, B.; Sun, L.; Wang, J.; Zhang, G.; Zhang, Y. W.; Shi, Y.; Wang, X. Towards Intrinsic Charge Transport in Monolayer Molybdenum Disulfide by Defect and Interface Engineering. *Nat. Commun.* **2014**, *5*, 5290.

(33) Szabó, Á.; Jain, A.; Parzefall, M.; Novotny, L.; Luisier, M. Electron Transport through Metal/MoS2 Interfaces: Edge- or Area-Dependent Process? *Nano Lett.* **2019**, *19*, 3641−3647.

(34) Park, W.; Min, J.-W.; Shaikh, S. F.; Hussain, M. M. Stable MoS2 Field-Effect Transistors Using TiO2 Interfacial Layer at Metal/MoS2 Contact. *Phys. Status Solidi A* **2017**, *214*, 1700534.

(35) Neupane, G. P.; Tran, M. D.; Yun, S. J.; Kim, H.; Seo, C.; Lee, J.; Han, G. H.; Sood, A. K.; Kim, J. Simple Chemical Treatment to n-Dope Transition-Metal Dichalcogenides and Enhance the Optical and Electrical Characteristics. *ACS Appl. Mater. Interfaces* **2017**, *9*, 11950−11958.

(36) Kufer, D.; Lasanta, T.; Bernechea, M.; Koppens, F. H. L.; Konstantatos, G. Interface Engineering in Hybrid Quantum Dot−2D Phototransistors. *ACS Photonics* **2016**, *3*, 1324−1330.

(37) Nan, F.; Li, P.; Li, J.; Cai, T.; Ju, S.; Fang, L. Experimental and Theoretical Evidence of Enhanced Visible Light Photoelectrochemical and Photocatalytic Properties in MoS2/TiO2 Nanohole Arrays. *J. Phys. Chem. C* **2018**, *122*, 15055−15062.

(38) Pak, Y.; Park, W.; Mitra, S.; Sasikala Devi, A. A.; Loganathan, K.; Kumaresan, Y.; Kim, Y.; Cho, B.; Jung, G.-Y.; Hussain, M. M.; Roqan, I. S. Enhanced Performance of MoS2 Photodetectors by Inserting an ALD-Processed TiO2 Interlayer. *Small* **2018**, *14*, 1703176.

(39) Lin, J.; Zhong, J.; Zhong, S.; Li, H.; Zhang, H.; Chen, W. Modulating Electronic Transport Properties of MoS2 Field Effect Transistor by Surface Overlayers. *Appl. Phys. Lett.* **2013**, *103*, 063109.

(40) Xu, K.; Wang, Y.; Zhao, Y.; Chai, Y. Modulation Doping of Transition Metal Dichalcogenide/Oxide Heterostructures. *J. Mater. Chem. C* **2017**, *5*, 376−381.

(41) Chuang, S.; Battaglia, C.; Azcatl, A.; McDonnell, S.; Kang, J. S.; Yin, X.; Tosun, M.; Kapadia, R.; Fang, H.; Wallace, R. M.; Javey, A. MoS2 P-type Transistors and Diodes Enabled by High Work Function MoOx Contacts. *Nano Lett.* **2014**, *14*, 1337−1342.

(42) Zhou, C.; Zhao, Y.; Raju, S.; Wang, Y.; Lin, Z.; Chan, M.; Chai, Y. Carrier Type Control of WSe2 Field-Effect Transistors by Thickness Modulation and MoO3 Layer Doping. *Adv. Funct. Mater.* **2016**, *26*, 4223−4230.

(43) Luo, W.; Zhu, M.; Peng, G.; Zheng, X.; Miao, F.; Bai, S.; Zhang, X.-A.; Qin, S. Carrier Modulation of Ambipolar Few-Layer MoTe2 Transistors by MgO Surface Charge Transfer Doping. *Adv. Funct. Mater.* **2018**, *28*, 1704539.

(44) Ho, P.-H.; Chang, Y.-R.; Chu, Y.-C.; Li, M.-K.; Tsai, C.-A.; Wang, W.-H.; Ho, C.-H.; Chen, C.-W.; Chiu, P.-W. High-Mobility InSe Transistors: The Role of Surface Oxides. *ACS Nano* **2017**, *11*, 7362−7370.

(45) Li, M.; Lin, C.-Y.; Yang, S.-H.; Chang, Y.-M.; Chang, J.-K.; Yang, F.-S.; Zhong, C.; Jian, W.-B.; Lien, C.-H.; Ho, C.-H.; Liu, H.-J.; Huang, R.; Li, W.; Lin, Y.-F.; Chu, J. High Mobilities in Layered InSe Transistors with Indium-Encapsulation-Induced Surface Charge Doping. *Adv. Mater.* **2018**, *30*, No. e1803690.

(46) Ghiasi, T. S.; Quereda, J.; van Wees, B. J. Bilayer h-BN Barriers for Tunneling Contacts in Fully-Encapsulated Monolayer MoSe 2 Field-Effect Transistors. *2D Mater.* **2018**, *6*, 015002.

(47) Hattori, Y.; Taniguchi, T.; Watanabe, K.; Nagashio, K. Determination of Carrier Polarity in Fowler−Nordheim Tunneling and Evidence of Fermi Level Pinning at the Hexagonal Boron Nitride/Metal Interface. *ACS Appl. Mater. Interfaces* **2018**, *10*, 11732−11738.

(48) Wei, T.; Lau, W. M.; An, X.; Yu, X. Interfacial Charge Transfer in $MoS_2/TiO_2$ Heterostructured Photocatalysts: The Impact of Crystal Facets and Defects. *Molecules* **2019**, *24*, 1769.

(49) Chen, B.; Meng, Y.; Sha, J.; Zhong, C.; Hu, W.; Zhao, N. Preparation of MoS2/TiO2 Based Nanocomposites for Photocatalysis and Rechargeable Batteries: Progress, Challenges, and Perspective. *Nanoscale* **2018**, *10*, 34−68.

(50) Kresse, G.; Furthmüller, J. Efficient Iterative Schemes for Ab initio Total-Energy Calculations using a Plane-wave Basis Set. *Phys. Rev. B: Condens. Matter Mater. Phys.* **1996**, *54*, 11169−11186.

(51) Grimme, S. Semiempirical GGA-type Density Functional Constructed with a Long-Range Dispersion Correction. *J. Comput. Chem.* **2006**, *27*, 1787−1799.

(52) Li, H.; Zhang, Q.; Yap, C. C. R.; Tay, B. K.; Edwin, T. H. T.; Olivier, A.; Baillargeat, D. From Bulk to Monolayer MoS2: Evolution of Raman Scattering. *Adv. Funct. Mater.* **2012**, *22*, 1385−1390.

(53) Lee, C.; Yan, H.; Brus, L. E.; Heinz, T. F.; Hone, J.; Ryu, S. Anomalous Lattice Vibrations of Single- and Few-Layer MoS2. *ACS Nano* **2010**, *4*, 2695−2700.

(54) Zhang, Q.; Ma, L.; Shao, M.; Huang, J.; Ding, M.; Deng, X.; Wei, X.; Xu, X. Anodic Oxidation Synthesis of One-Dimensional TiO2 Nanostructures for Photocatalytic and Field Emission Properties. *J. Nanomater.* **2014**, *2014*, 1−14.

(55) Yang, L.; Majumdar, K.; Liu, H.; Du, Y.; Wu, H.; Hatzistergos, M.; Hung, P. Y.; Tieckelmann, R.; Tsai, W.; Hobbs, C.; Ye, P. D. Chloride Molecular Doping Technique on 2D Materials: WS2 and MoS2. *Nano Lett.* **2014**, *14*, 6275−6280.

(56) Lin, J. D.; Han, C.; Wang, F.; Wang, R.; Xiang, D.; Qin, S.; Zhang, X.-A.; Wang, L.; Zhang, H.; Wee, A. T. S.; Chen, W. Electron-Doping-Enhanced Trion Formation in Monolayer Molybdenum Disulfide Functionalized with Cesium Carbonate. *ACS Nano* **2014**, *8*, 5323−5329.

(57) Smidstrup, S.; Markussen, T.; Vancraeyveld, P.; Wellendorff, J.; Schneider, J.; Gunst, T.; Verstichel, B.; Stradi, D.; Khomyakov, P. A.; Vej-Hansen, U. G.; Lee, M.-E.; Chill, S. T.; Rasmussen, F.; Penazzi, G.; Corsetti, F.; Ojanperä, A.; Jensen, K.; Palsgaard, M. L. N.; Martinez, U.; Blom, A.; Brandbyge, M.; Stokbro, K. QuantumATK: An Integrated Platform of Electronic and Atomic-Scale Modelling Tools. *J. Phys.: Condens. Matter* **2020**, *32*, 015901.

(58) Smidstrup, S.; Stradi, D.; Wellendorff, J.; Khomyakov, P. A.; Vej-Hansen, U. G.; Lee, M.-E.; Ghosh, T.; Jónsson, E.; Jónsson, H.; Stokbro, K. First-Principles Green's-Function Method for Surface Calculations: A Pseudopotential Localized Basis Set Approach. *Phys. Rev. B* **2017**, *96*, 195309.

(59) Korn, T.; Heydrich, S.; Hirmer, M.; Schmutzler, J.; Schüller, C. Low-Temperature Photocarrier Dynamics in Monolayer MoS2. *Appl. Phys. Lett.* **2011**, *99*, 102109.

(60) Elsaesser, T.; Shah, J.; Rota, L.; Lugli, P. Initial Thermalization of Photoexcited Carriers in GaAs Studied by Femtosecond Luminescence Spectroscopy. *Phys. Rev. Lett.* **1991**, *66*, 1757−1760.

(61) Das, S.; Gupta, G.; Majumdar, K. Layer Degree of Freedom for Excitons in Transition Metal Dichalcogenides. *Phys. Rev. B* **2019**, *99*, 165411.

(62) Sim, S.; Park, J.; Song, J.-G.; In, C.; Lee, Y.-S.; Kim, H.; Choi, H. Exciton Dynamics in Atomically Thin MoS2: Interexcitonic Interaction and Broadening Kinetics. *Phys. Rev. B: Condens. Matter Mater. Phys.* **2013**, *88*, 075434.

(63) Sharma, R.; Aneesh, J.; Yadav, R. K.; Sanda, S.; Barik, A. R.; Mishra, A. K.; Maji, T. K.; Karmakar, D.; Adarsh, K. V. Strong Interlayer Coupling Mediated Giant Two-Photon Absorption in MoSe2/ Graphene Oxide Heterostructure: Quenching of Exciton Bands. *Phys. Rev. B* **2016**, *93*, 155433.

(64) Yadav, R. K.; Aneesh, J.; Sharma, R.; Abhiramnath, P.; Maji, T. K.; Omar, G. J.; Mishra, A. K.; Karmakar, D.; Adarsh, K. V. Designing Hybrids of Graphene Oxide and Gold Nanoparticles for Nonlinear Optical Response. *Phys. Rev. Appl.* **2018**, *9*, 044043.

(65) Gupta, G.; Kallatt, S.; Majumdar, K. Direct Observation of Giant Binding Energy Modulation of Exciton Complexes in Monolayer MoSe2. *Phys. Rev. B* **2017**, *96*, No. 081403(R).

(66) Clement, C. E.; Jiang, D.; Thio, S. K.; Park, S.-Y. A Study of Dip-Coatable, High-Capacitance Ion Gel Dielectrics for 3D EWOD Device Fabrication. *Materials* **2017**, *10*, 41.

(67) Taghavikish, M.; Subianto, S.; Gu, Y.; Sun, X.; Zhao, X. S.; Choudhury, N. R. A Poly(ionic liquid) Gel Electrolyte for Efficient all Solid Electrochemical Double-Layer Capacitor. *Sci. Rep.* **2018**, *8*, 10918.

(68) Mondal, S.; Ram Ghimire, R.; Raychaudhuri, A. K. Enhancing Photoresponse by Synergy of Gate and Illumination in Electric Double Layer Field Effect Transistors Fabricated on n-ZnO. *Appl. Phys. Lett.* **2013**, *103*, 231105.